

Computational fluid dynamics analysis of cold plasma carrier gas injected into a fluid using level set method

Mehrdad Shahmohammadi Beni and K. N. Yu^{a)}

Department of Physics and Materials Science, City University of Hong Kong, Kowloon Tong, Hong Kong

(Received 11 August 2015; accepted 1 October 2015; published 14 October 2015)

A promising application of plasma medicine is to treat living cells and tissues with cold plasma. In cold plasmas, the fraction of neutrals dominates, so the carrier gas could be considered the main component. In many realistic situations, the treated cells are covered by a fluid. The present paper developed models to determine the temperature of the fluid at the positions of the treated cells. Specifically, the authors developed a three-phase-interaction model which was coupled with heat transfer to examine the injection of the helium carrier gas into water and to investigate both the fluid dynamics and heat transfer output variables, such as temperature, in three phases, i.e., air, helium gas, and water. Our objective was to develop a model to perform complete fluid dynamics and heat transfer computations to determine the temperature at the surface of living cells. Different velocities and plasma temperatures were also investigated using finite element method, and the model was built using the COMSOL MULTIPHYSICS software. Using the current model to simulate plasma injection into such systems, the authors were able to investigate the temperature distributions in the domain, as well as the surface and bottom boundary of the medium in which cells were cultured. The temperature variations were computed at small time intervals to analyze the temperature increase in cell targets that could be highly temperature sensitive. Furthermore, the authors were able to investigate the volume of the plasma plume and its effects on the average temperature of the medium layer/domain. Variables such as temperature and velocity at the cell layer could be computed, and the variations due to different plume sizes could be determined. The current models would be very useful for future design of plasma medicine devices and procedures involving cold plasmas. © 2015 American Vacuum Society. [<http://dx.doi.org/10.1116/1.4933107>]

I. INTRODUCTION

Plasma medicine is a new and fast growing field. There are many excellent reviews on this topic (e.g., Refs. 1–3). *Biointerphases* has recently published a timely special issue on plasma medicine, in which Graves *et al.* summarized the latest research results in the editorial.⁴ One of the most promising applications of plasma medicine is to treat living cells and tissues with cold plasma (e.g., Refs. 5–12). Broadly speaking, plasmas can be classified into hot plasma (or thermal plasma) and cold plasma (or nonthermal plasma) according to the relative temperatures of the electrons, ions, and neutrals. While electrons and other particles in a hot plasma are in thermal equilibrium (i.e., they have the same temperature), the electrons in a cold plasma have a much higher temperature than those of the other particles (the latter approximately at room temperature). The degree of ionization in a cold plasma is also much lower than that in a hot plasma. Cold plasmas are conveniently generated through dielectric barrier discharge and corona discharge.¹³ The thermal tolerance of living cells and tissues is a crucial factor for consideration when designing devices and procedures for applying plasma medicine. For example, Tiede *et al.* pointed out that temperatures beyond 40 °C would lead to detrimental effects in cells.¹⁴ Usually, temperatures lower

than the human body temperature are required for successful biomedical applications. However, as of today, relatively few studies have been devoted to examine the characteristics of temperature changes at the surface of living cells and tissues during plasma treatment. Schröder *et al.* was one of the pioneer groups who formulated a parameterized model, which could be employed to simulate the species densities generated by a plasma needle and the corresponding heat transfer to a skin layer.¹⁵ The input parameters included the power dissipation, discharge gap, and the geometry of the employed plasma needle.

The model of Schröder *et al.*¹⁵ was very helpful in that it could be used, for example, to optimize the species densities while maintaining an acceptable skin temperature during the plasma treatment, and to optimize the design of the plasma medical devices. In many other realistic situations, however, the treated cells are covered on top by a fluid so the plasma would first come into contact with this fluid. Furthermore, the temperature of the fluid at the positions of the treated cells would then be determined by the depth, heat conductivity, as well as heat capacity of the fluid above the treated cells, in addition to other factors, including the temperature and pressure of the plasma, dimensions, and velocity of the plasma flame. As such, it is necessary to develop another model to take care of these factors, which is the main objective of the present paper.

In this paper, we studied cold plasmas generated by a helium (He) gas. Helium is a favorable carrier gas due to its

^{a)} Author to whom correspondence should be addressed; electronic mail: peter.yu@cityu.edu.hk

low breakdown voltage and the uniformity of its generated plasmas.¹⁶ Since cold plasmas are dominated by the neutral He atoms, their thermofluid properties can be surrogated by those of the He carrier gas. The carrier gas provided a pathway for the ions and free radicals to come into contact with the treated cells. We developed a three-phase-interaction model, which was coupled with heat transfer to examine the injection of the He carrier gas into water and to investigate both the fluid dynamics and heat transfer parameters in three phases, i.e., air, helium gas, and water.

Experimental validation is important for such modeling studies. Despite that the study in Ref. 15 was a pure numerical simulation, the authors highlighted the importance of experimental validation. In the present work, we used the experimental setup of and data from Akhlaghi *et al.*¹⁶ for our model inputs. In particular, the authors measured the temperature of the plasma plume at different distances from the nozzle outlet and showed that at higher voltages the temperature in different sections of plasma plume changed, generating a temperature gradient.¹⁶ The different temperature profiles were first simulated for use in our model.

The significance of our work was to perform complete fluid dynamics computation and to examine the effect of heat transfer on the performance and efficiency of the studied systems. Furthermore, a variety of different velocities and plasma temperatures were studied using the finite element method (FEM), and the model was built using the COMSOL MULTIPHYSICS software.

II. DESCRIPTION OF THE MODELS

A. Variation of temperature with distance from nozzle

For our model, we employed the experimental data from Akhlaghi *et al.* on the temperature of the plasma plume that were measured at different distances away from the nozzle outlet.¹⁶ The length of the plasma plume, which was generated in their experiment, was ~ 20 mm when measured from the outlet of the nozzle. We simulated a section of the plasma from 15 to 20 mm away from the nozzle outlet due to the lesser variations of the temperature here when compared to the sections closer to the nozzle outlet and also due to the availability of experimental data. In reality, when the plasma plume came into contact with small targets such as cells and the covering liquid medium, only a small section of the plasma plume was involved, so we focused on a small section of the plume with a length of only 5 mm to examine the thermal effect on the cells and the medium. For different applied voltages to the nozzle, the temperature of the plasma would vary, which was clearly observed at voltages higher than 4 kV in the experiments. As such, we also considered this effect in our numerical computations using empirical fits to the experimental data from Fig. 3 in Ref. 16, namely,

$$\text{At 6 kV: } f_{6\text{kV}}(z) = (-0.2z + 38)^\circ\text{C} \quad 15 \text{ mm} \leq z \leq 20 \text{ mm}, \quad (1)$$

$$\text{At 5 kV: } f_{5\text{kV}}(z) = 30^\circ\text{C} \quad 15 \text{ mm} \leq z \leq 20 \text{ mm}, \quad (2)$$

$$\text{At 4 kV: } f_{4\text{kV}}(z) = 28^\circ\text{C} \quad 15 \text{ mm} \leq z \leq 20 \text{ mm}, \quad (3)$$

$$\text{At 3 kV: } f_{3\text{kV}}(z) = 27^\circ\text{C} \quad 15 \text{ mm} \leq z \leq 20 \text{ mm}, \quad (4)$$

where $f(z)$ was the temperature as a function of distance z from the nozzle outlet.

B. Grid systems

In our model, we introduced a grid system to couple two grids containing fluids at different phases or states of matter such as a gas and a liquid. This was achieved by placing two different domains in contact and couple their physics by defining proper boundary conditions at their interfaces and solving the Navier–Stokes momentum equations with continuity equations individually for different fluids in their respective domains, so that three different fluids were able to interact continuously when the dependent variables such as pressure, temperature, and velocity were fully coupled. In the beginning, grid 1 contained two fluids which were air and helium gas; while grid 2 contained water which was stationary. The initial temperature and pressure of air and water were 25°C and 1 atm, respectively, and the plasma was located in the air domain at $1 \mu\text{m}$ above the water medium as shown in Fig. 1, and we used different temperatures which corresponded to different voltages. Through numerically solving the level set function in grid 1, we could track and identify different phases as the helium gas moved downwards to enter the water domain. The heat equation was used to describe the heat transfer in the fluids which were present in both grids, and both the fluid mechanics and heat transfer models were coupled and solved using a time dependent solver. It was necessary to have a multiphysics system as described here due to the nature of the materials involved in this computation. In the presence of gases with temperature- and pressure-dependent properties such as the density, the temperature should be carefully monitored as heat was transferred from the plume to other sections of grids 1 and 2.

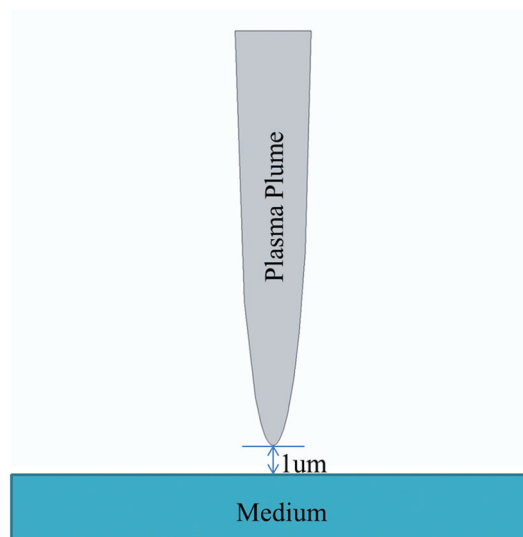


FIG. 1. Plasma plume above the medium surface.

TABLE I. Summary of grids containing different fluids.

Domain	Grid No.	Geometry	Dimensions
Air	1	Cylinder	10 mm radius × 12.8 mm height
Water	2	Cylinder	10 mm radius × 0.30 mm height

C. Geometry of the system

The overall geometry and dimensions of our system are summarized in Table I and Fig. 2. The plasma was located in grid 1, and the geometry was approximated using a semiprolate spheroid with a circular base. It would be difficult and tedious to experimentally determine the exact plume geometry, but a bullet shape semiprolate spheroid would be a reasonable approximation. When the plasma exited from the nozzle and discharged in air, since the plasma plume density was smaller than the air density, contacts between the plasma and air molecules reduced the plasma velocity at sections furthest away from the plume centerline, which led to such bullet shape geometries. The two main parameters were *a* and *b*, as shown in Fig. 3. The volume of the semispheroid was

$$V = \frac{1}{2} \left(\frac{4}{3} \pi r^2 \times a \right), \tag{5}$$

where $b = 2r$. In our case, the height *a* of the plasma plume was much longer than the radius of the circular bases *r* (i.e., $a \gg r$), so the surface area excluding the circular base area was

$$S = \pi r^2 \left(1 + \frac{a}{re} \sin^{-1} e \right), \quad \text{where } e = \sqrt{1 - \frac{r^2}{a^2}}. \tag{6}$$

Typical geometries of plasma plumes with different circular-base diameters are shown in Table II. It is remarked here that *a* was taken to be 5 mm, as we considered a section of the plasma from 15 to 20 mm away from the nozzle outlet as described above.

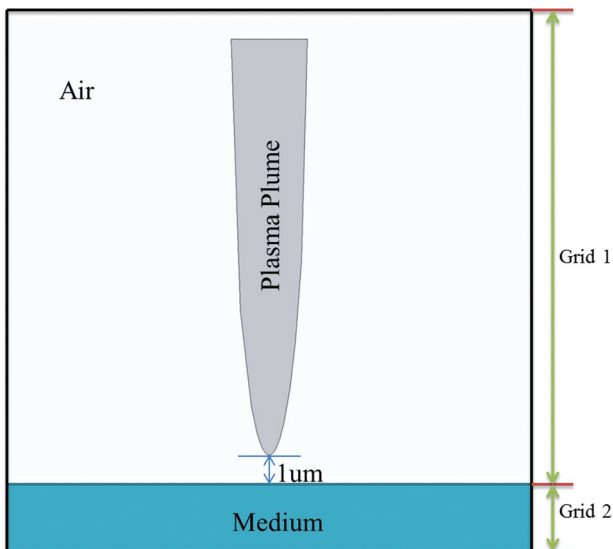


FIG. 2. Schematic diagram of system setup and grid system.

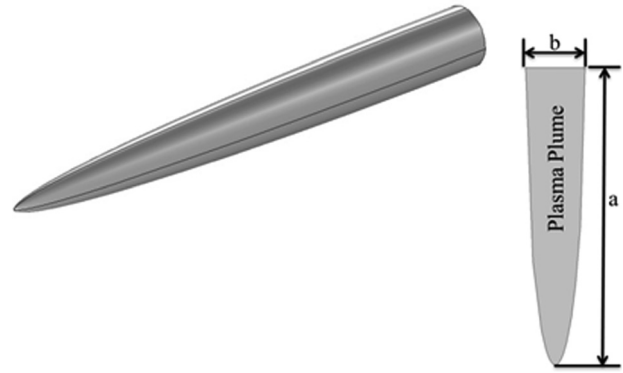


FIG. 3. Simulation of plume by a semiprolate spheroid.

In order to characterize the initial contact of the carrier gas with the liquid medium, we numerically computed the curvature length of the plasma plume by considering a length of 50 μm measured from the tip of semiprolate spheroid, as shown in Fig. 4. The results are summarized in Table III. This procedure was adopted to replace the use of the contact angle, and as such, the curvature arc length could be considered as a contact length. The contact length was only measured and tabulated in Table III before simulation started and before the plume interacted with the air and the medium. Later, when the plasma plume moved downwards, it entered and traveled in the medium. The curvature length would change as the geometry of the plume changed. It is remarked here that the slip boundary condition was applied for the boundary of the plasma plume so that it could move downwards in the air domain.

D. Fluid dynamics model

The standard gas flow rate used in the experimental setup was 4 l/min, which was ejected out from a circular diameter of 6 mm, so the flow speed was 2.3579 m/s. The downward initial velocity of our carrier gas was set to be the same as the one used in the real experiments so that further comparisons could be made between other variables. The initial velocity of the plasma plume acted as a push to initialize the motion of the plume which was in this case a volume that moved and interacted with the surrounding air and the underneath medium.

Three fluids were involved in our model, namely, helium (gas), air (gas), and water (liquid). Air and helium gas were considered to behave as ideal gases. The pressure of the whole system was set to be 1 atm, and the temperatures of the helium carrier gas were fixed for different operating voltages using Eqs. (1)–(4). By rearranging the ideal gas law, the densities of air and helium gas could be determined from

TABLE II. Geometries of plasma plumes with different circular-base diameters.

No.	<i>b</i> (mm)	Volume (mm ³)	Surface area (mm ²)
1	0.2	0.1047	2.4679
2	0.4	0.4189	4.9386
3	0.6	0.9425	7.4149

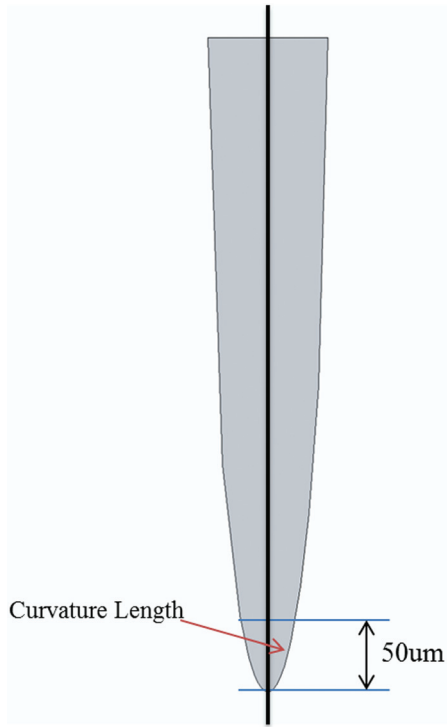


FIG. 4. Geometry for numerical computation of the curvature arc length.

$$\rho(T, P) = \frac{PM}{RT}, \quad (7)$$

where P was the system pressure, M was the molar mass of the gases, and R was the gas constant.

The level set function was used to track the evolution of the moving interface between the helium gas and air in grid 1. There was no continuous fluid flowing out of the nozzle so the volume of the helium gas initially present in grid 1 was constant. The level set method enabled us to track the evolution of phases (helium gas and air). The level set function controlled the interface thickness between the two gases and took care of the mixing between them as helium moved through the air domain. An added advantage of using the level set method was that the current model could be extended in future works to investigate ion transport and electron density, etc., and it would be realistic to have the plasma plume moving while we explored the interaction of ions with the medium and the surrounding air in detail. The velocity field of helium, which had a moving interface with air, was \mathbf{u} as shown in the following equation:

$$\frac{\partial \phi}{\partial t} + \mathbf{u} \cdot \nabla \phi = \gamma \nabla \cdot \left(\varepsilon \nabla \phi - \phi(1 - \phi) \frac{\nabla \phi}{|\nabla \phi|} \right). \quad (8)$$

TABLE III. Curvature arc lengths at the tip of plume.

No.	b (mm)	Length (mm)
1	0.2	0.0517
2	0.4	0.0586
3	0.6	0.0675

The function $[(\partial \phi / \partial t) + \mathbf{u} \cdot \nabla \phi]$ described the motion of the interface between the carrier gas and air, and was known as the evolution function when it was equated to zero. Furthermore, in Eq. (8), the thickness of the region where the level set function varied mainly from 0 to 1 would be determined by ε , and in our model, this parameter was set to be 0.2228, which was equivalent to the largest mesh size in the helium gas domain. The terms were multiplied with γ for better numerical stability, where γ reduced the oscillations in the level set function and kept the interface thickness constant. As described above, the evolution function was given by

$$\frac{\partial \phi}{\partial t} + \mathbf{u} \cdot \nabla \phi = 0. \quad (9)$$

The slip boundary condition was applied along the initial interface surrounding the helium carrier gas, which allowed the carrier gas to move relative to the stationary medium. The initial interface around the carrier gas domain would set the boundaries of the semispheroid plume as the initial position for the level set function, which was mathematically expressed as

$$\phi = 0. \quad (10)$$

The boundary conditions used in the present work were as follows. In grid 1, since the air and plasma plume were in contact and the plasma plume moved downwards in the air domain, the slip boundary condition was used between them. Similarly, at the upper boundary of the medium (grid 2), which was in contact with grid 1, the slip boundary condition was also adopted. However, the no-slip boundary condition was applied at the bottom of grid 2 due to the higher adhesive forces between fluid–solid interfaces than cohesive forces between the fluid particles. In reality, adherent cells would attach to and would remain stationary with respect to the bottom of the culture dish.

E. Heat transfer and fluid dynamic models

The continuity equation (for compressible fluids) defined in Grid 1, which contains compressible fluids, is given by

$$\frac{\partial \rho}{\partial t} + \nabla \cdot (\rho \mathbf{u}) = 0. \quad (11)$$

The continuity equation (for incompressible fluids) defined in grid 2 which contains water under normal conditions is given by

$$\rho \nabla \cdot \mathbf{u} = 0. \quad (12)$$

Water in grid 2 was assumed to be an incompressible fluid, with a fixed density of 1 g cm^3 . The Navier–Stokes momentum equation is given by

$$\rho \frac{\partial \mathbf{u}}{\partial t} + \rho \mathbf{u} \cdot \nabla \mathbf{u} = -\nabla P + \nabla \cdot \left[\mu (\nabla \mathbf{u} + (\nabla \mathbf{u})^T) - \frac{2}{3} \mu (\nabla \cdot \mathbf{u}) \mathbf{I} \right] + \mathbf{F}, \quad (13)$$

where ρ is density, P is pressure, u is the velocity of the flow, F is given by $F = \rho g + F_{st} + F_{vf}$, ρg is the body force, F_{st} is the surface tension, and F_{vf} is the volume force. We neglected the surface tension of water and the body force in grid 1, as grid 1 contained gases which had relatively low densities at the mentioned temperatures and pressure, so the effect of the body force would be negligible. Equation (13) is applicable for both compressible and incompressible fluids. In grid 1, both of the fluids were considered compressible. However, the air in grid 1 was considered stationary when the experiment started, which corresponded to the assignment of a zero velocity to the air domain initially. This was justified when the real-life experiment was conducted in a controlled environment so that the air surrounding the medium/cells and the plasma plume had no velocity and was thus stationary in the beginning. As the plasma plume moved downwards, the surrounding air also moved, as there was a drag and some mixing between the two gases. The computed velocity variations were solely due to the motion of plume in the air domain. Such variations would be comparatively small when the carrier gas moved downwards. In addition, both the pressure and temperature were sufficiently low that the variations in the properties of air could be negligible.

In order to couple the two grids which contained different phases, the continuity and Navier–Stokes momentum equations were solved for each phase individually. The velocity field and pressure for each phase were coupled together so that the plasma plume could enter the medium from grid 1 to grid 2. Mass conservation and momentum equations as shown before were used to ensure a controlled volume, and boundary conditions described above were applied to allow interaction between helium and the medium.

Heat conduction and convection were introduced to simulate the heat transfer. Here, a constant temperature was applied to the plasma section according to the proposed empirical relations described in Eqs. (1)–(4). As such, when the plasma was injected into the medium, the temperature distribution would be kept constant so the temperature of the plume maintained its value over the entire simulation duration. The heat equation is given by

$$\rho c_p \frac{\partial T}{\partial t} + \rho c_p u \cdot \nabla T = -\nabla \cdot \phi + Q, \tag{14}$$

where $\phi = k\nabla T$, T is the temperature, c_p is the heat capacity at constant pressure, and k is the thermal conductivity. The system is time dependent so the temperature of the system will change with time. This approach was required for monitoring the temperature rise in the medium when the plasma carrier gas had to reach the treated cells located at a certain depth of the medium. Furthermore, thermal insulation was applied to the outer boundaries of grids 1 and 2 to stop heat flux across the boundaries in the system to ensure that the grids were “confined,” i.e.,

$$-n \cdot (-k\nabla T) = 0, \tag{15}$$

where n was the normal to the surface of the outer boundaries.

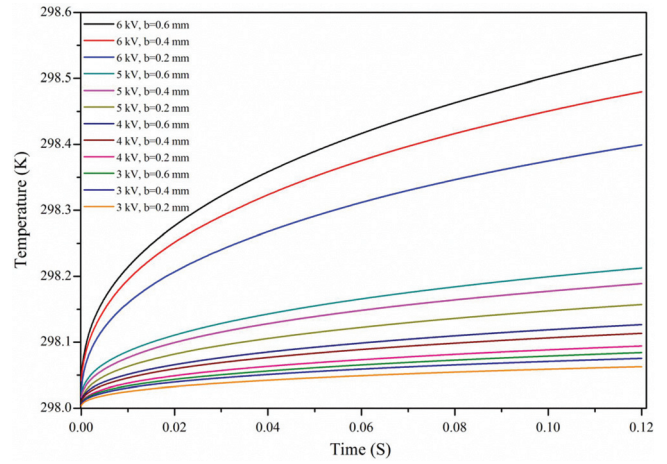


FIG. 5. Variation of average air temperature with time as the carrier gas moves into the medium through surrounding air.

In our model, the only heat source was the plasma carrier gas with a temperature defined by Eqs. (1)–(4). No other heat sources were considered so that the effects could be more clearly defined.

III. RESULTS AND DISCUSSION

The output results from our models could be classified into two major categories which were (1) related to heat transfer and fluid dynamics, (2) temperature changes measured as a function of time and distance (the latter being the width of grid 1). Furthermore, through horizontal probes, it was possible to observe the effects when the carrier gas was getting injected into the medium, which was initially at room temperature. The fluid dynamics related results helped demonstrate the effect of the helium carrier gas on the liquid medium and vice versa.

The variations of air temperature with time are shown in Fig. 5. Here, the simulations were performed up to 0.12 s so the instantaneous effect of the carrier gas injection could be observed more clearly. Since in reality the application time of the plasma could vary for different users, it would not be practical to simulate all possibilities. Our intention here was to

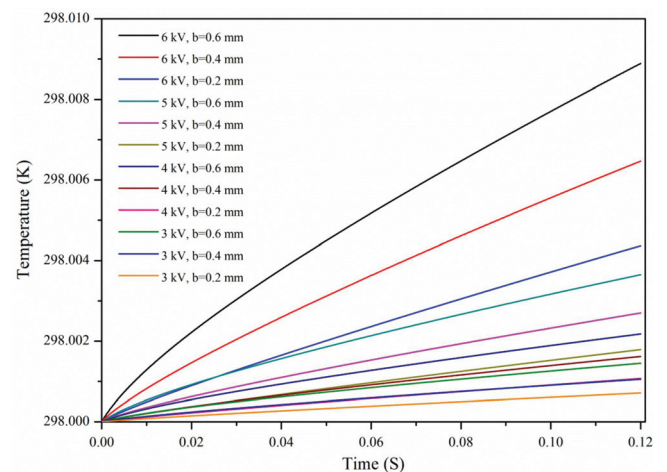


FIG. 6. Variation of average water temperature with time as the carrier gas moves into the medium.

identify the overall trend with special attention to the fastest changing part, which corresponded to the instantaneous effect (shown in Fig. 5 to occur at time <0.04 s). The choice of a small step size of 10^{-4} s would help identify this fastest changing part. As shown in Fig. 5, the trend showed stabilization or

saturation for the time beyond 0.04 s. Once the overall trend was identified, the final temperature (or at least its upper limit) for different applications could be estimated. A longer simulated period would either mean a loss in the time resolution, i.e., larger step size, or a longer computation time.

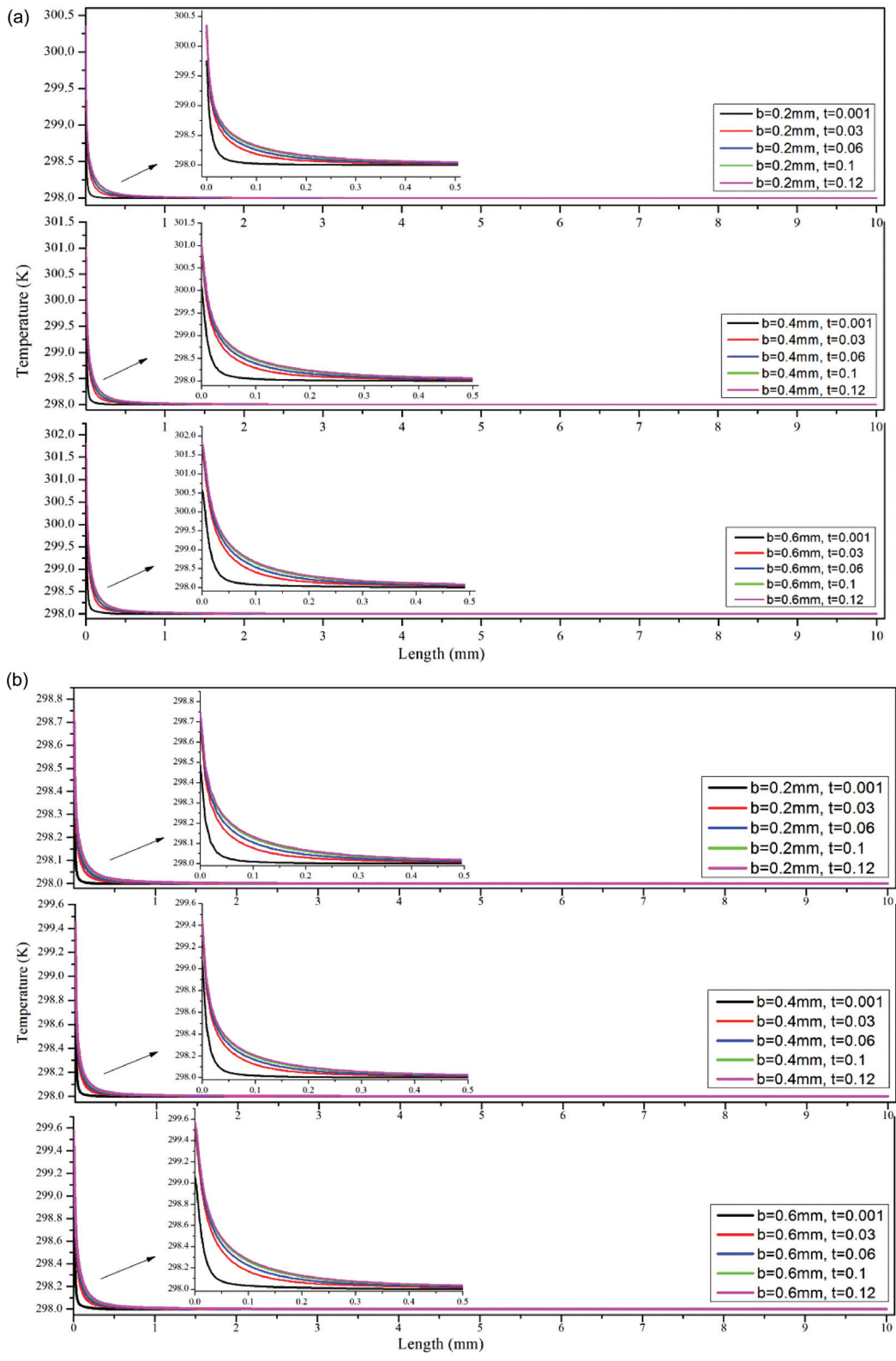


FIG. 7. Temperature of gas-liquid interface measured at different time vs interface length at (a) 6 kV, (b) 5 kV, (c) 4 kV, and (d) 3 kV operating voltage.

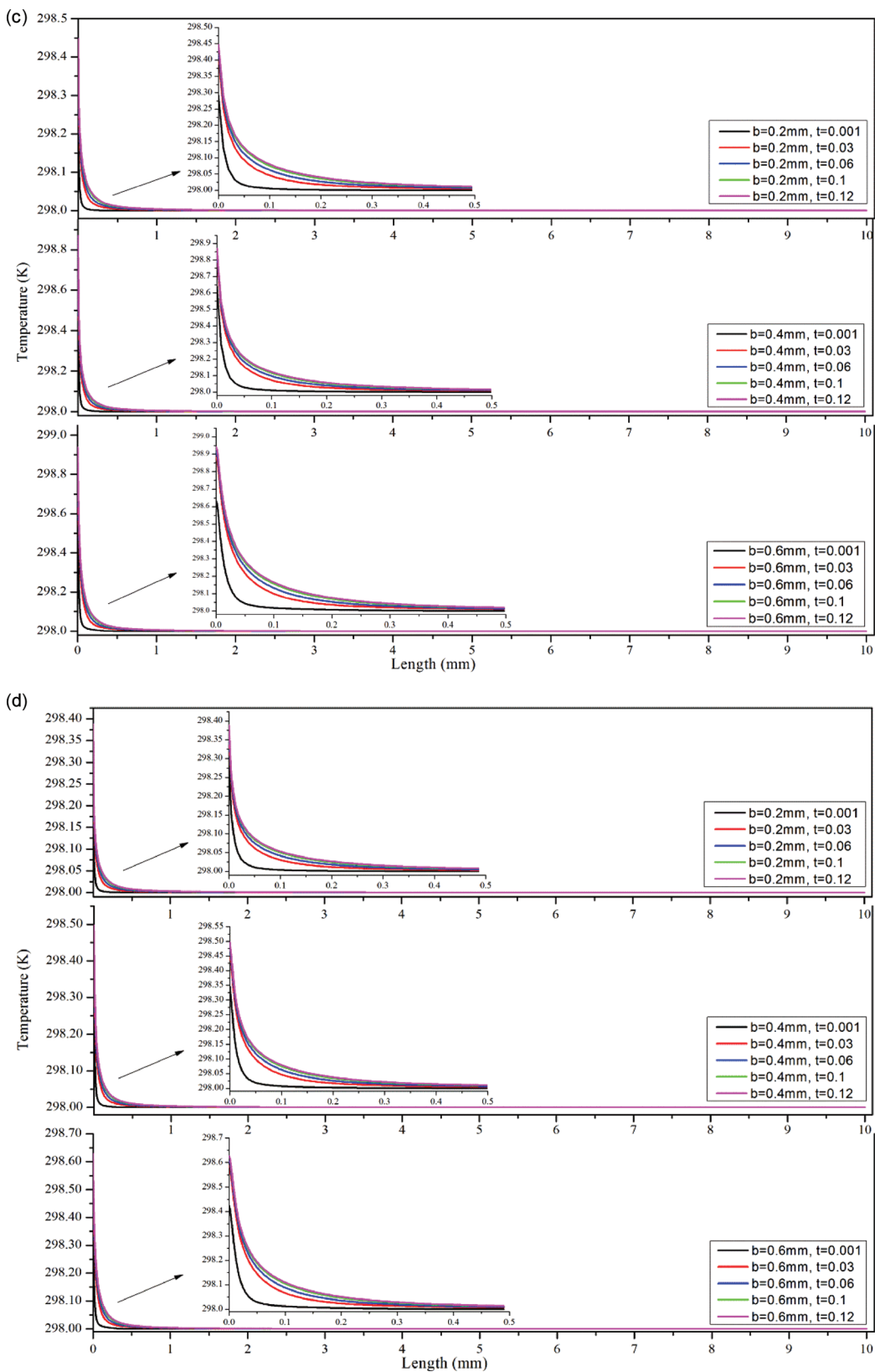


FIG. 7. (Continued).

Different base diameters b for the semiprolate spheroid were studied, which corresponded to different outlet nozzle diameters as well as different volumes of the helium carrier

gas. For the current model, the length of the plume was kept constant, so the geometry of the plume discharged out from the nozzle would change with b . The results showed that for

plasma plumes with larger volumes and contact curvature lengths (corresponding to larger b values), the temperature increases in the air domain were larger. The temperature rises for the operating voltage of 6 kV were much larger when compared with the other voltages, while the trends for the other curves were similar. This can be explained by the variation of the plasma plume temperature with the plume

length [see Eq. (1)] for the operating voltage of 6 kV, and the constant plasma plume temperature [see Eqs. (2)–(4)] for lower operating voltages.

The variations of water temperature with time are shown in Fig. 6. The water temperature increased when the carrier gas entered the liquid medium, but the increases were much smaller than those in the surrounding air. An

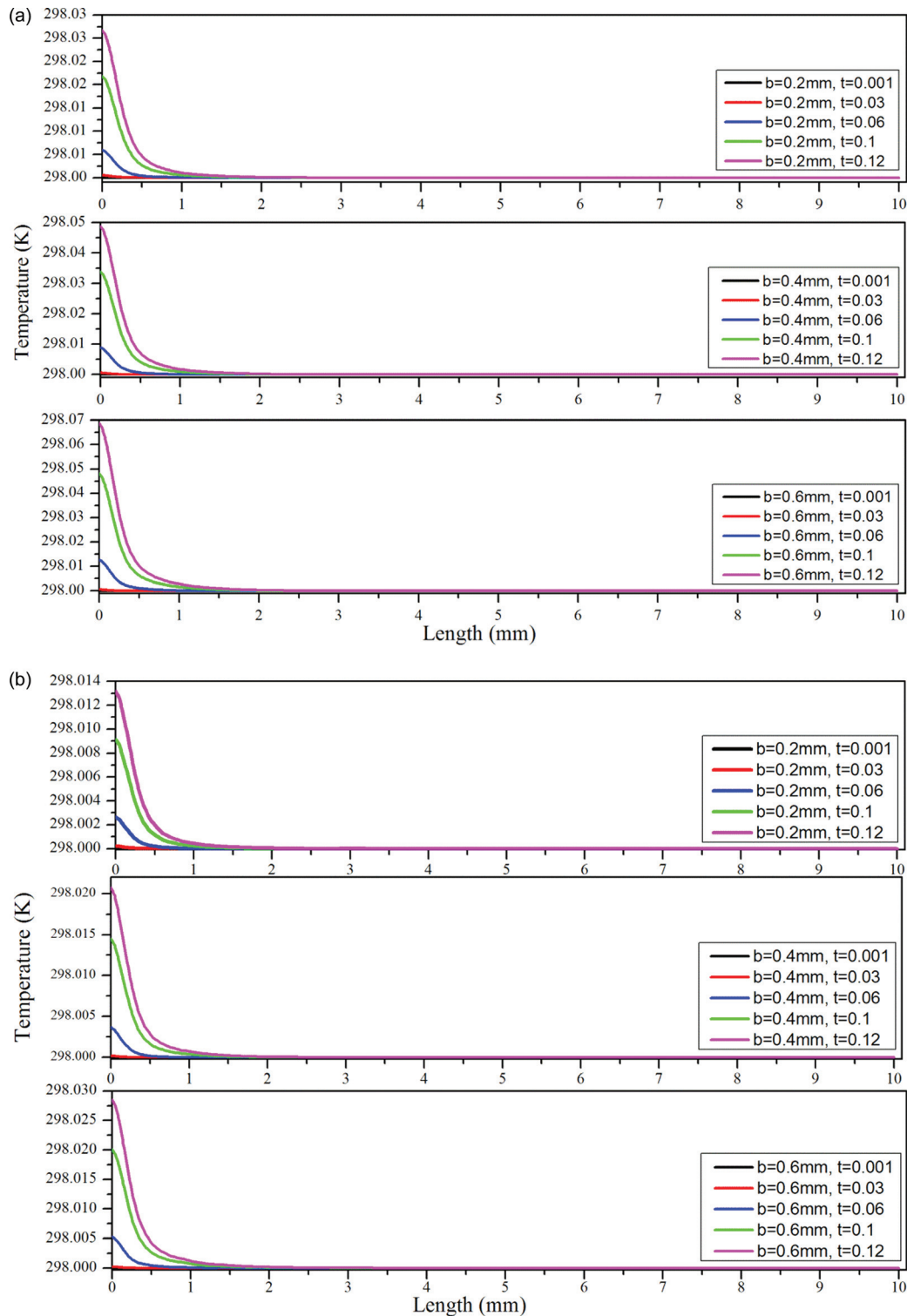


FIG. 8. Temperature at the bottom of liquid medium vs interface length at (a) 6 kV, (b) 5 kV, (c) 4 kV, and (d) 3 kV operating voltage.

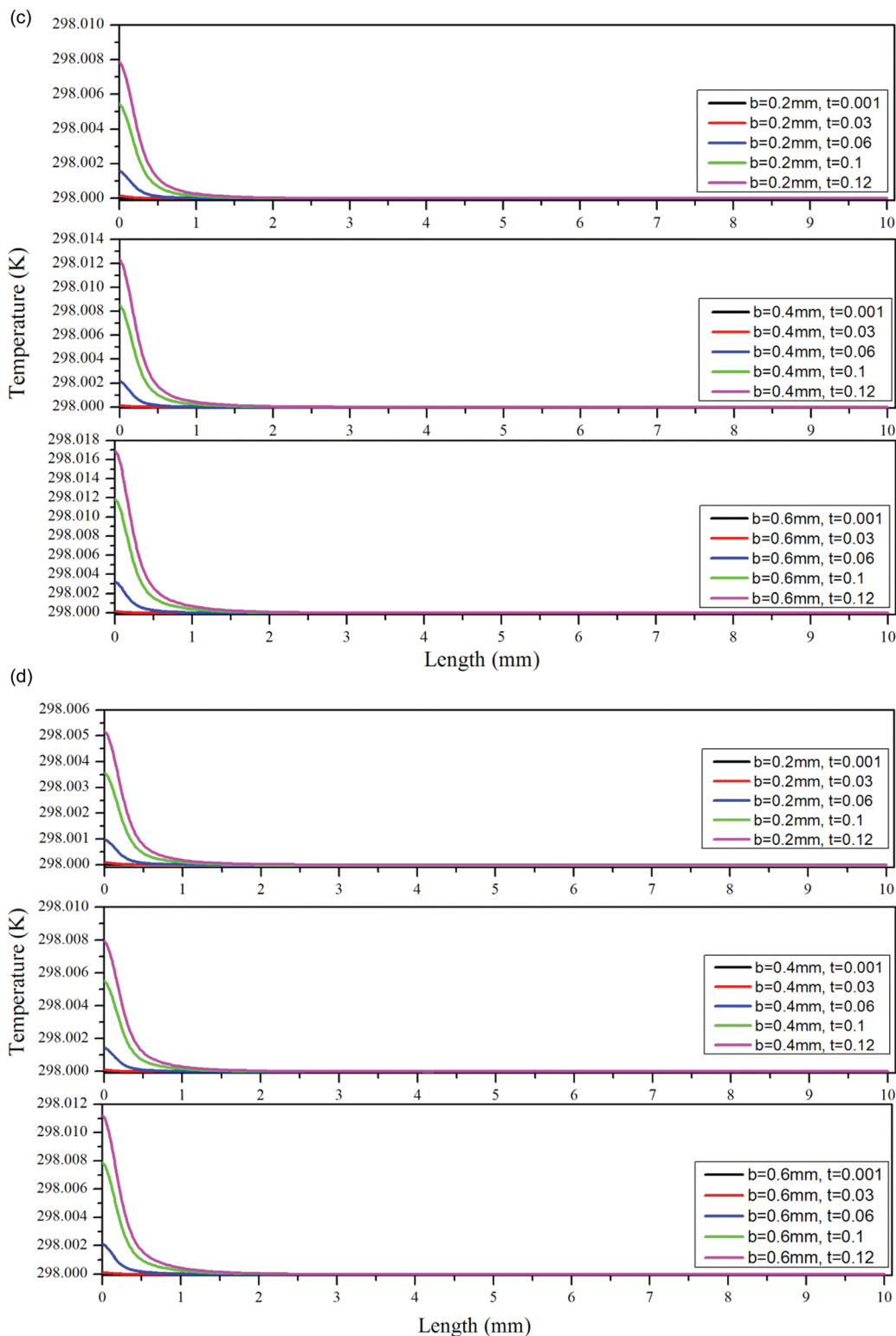


FIG. 8. (Continued).

important reason was that, for the simulated time duration, not all helium gas entered the medium as the carrier gas was abruptly slowed down upon contact with the medium interface. Initially, the plume was placed $1\ \mu\text{m}$ above the medium interface. As the plasma plume moved downwards, the first interaction between the tip of the plume

with the medium occurred at 4.24×10^{-7} s. The plume then continued to move downwards and entered the medium. The velocity of plasma plume was reduced as it continued to enter the underneath water, and its velocity reduction was shown in Fig. 10 for different plume volumes and temperatures.

Figures 7(a)–7(d) show the changes in the temperature of the gas–liquid interface for different operating voltages and b values in more details. Upon contact between the plasma and the liquid medium, heat energy was transferred to the medium surface. In addition, heat from the surrounding air could also increase the temperature of the medium interface due to the coupling between the two grids.

The bottom temperature of the liquid medium was also crucial as the cells would be located at the bottom during realistic plasma treatments. As such, the temperature changes at the bottom boundary of the water domain were computed as a function of the horizontal length, and the results were shown in Figs. 8(a)–8(d).

Figure 9 shows the variation of the air velocity with time as a result of plasma injection. Both plasma and air were present in grid 1 so the air which was initially stationary would move when the plasma moved downwards. The curves with the same b values overlapped with one another, which meant the major factor that controlled the air velocity was the volume of the plasma plume. A larger volume of the helium carrier gas would drive the air more strongly when the plasma moved downwards and entered the medium.

Figure 10 shows the variation of the plasma plume velocity with time for different voltages and volumes. Again, the velocity change of the helium carrier gas was essentially related to the volume of the plume, which was controlled by the parameter b . The plume velocity was significantly decreased when the plume came into contact with the medium surface, and this reduction upon impact was more conspicuous for plumes with smaller volumes or b values.

The volume fractions of helium carrier gas and air in grid 1 would change when the plume moved downwards in air and was injected into water medium. The level set method and conservation law were employed to track the volume fractions and their evolution. The results were shown in Figs. 11(a) and 11(b), which showed that the air volume fraction was much larger than the helium gas volume fraction. This difference was justified considering that the plasma plume had a relatively smaller volume when

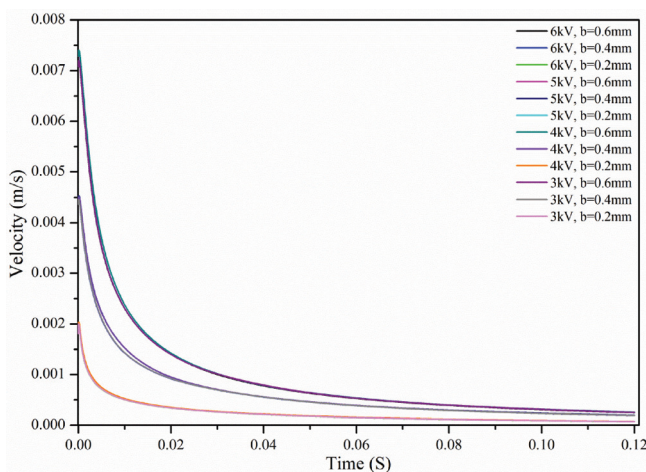


Fig. 9. Variation of average air velocity with time as a result of plasma injection.

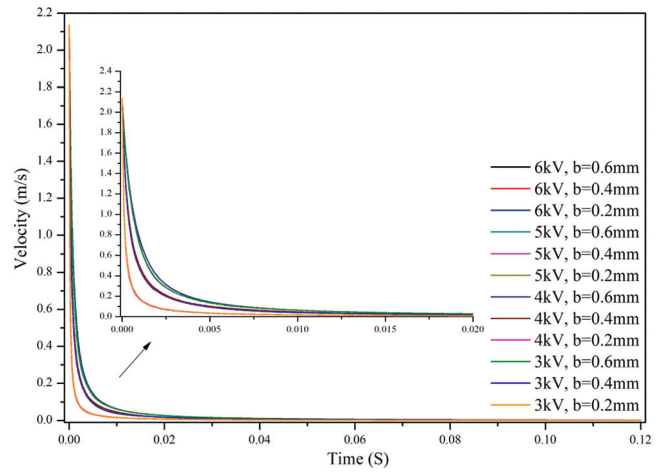


Fig. 10. Variation of average plasma plume velocity with time for different voltages and volumes.

compared to air, and that the volume fraction was defined as the ratio between the volume of the considered component and the total volume of the system. The same reasoning would also be valid when the plasma was injected into the medium through the surrounding air.

The velocities at the medium interface were also determined to assess the impact of the helium carrier gas on

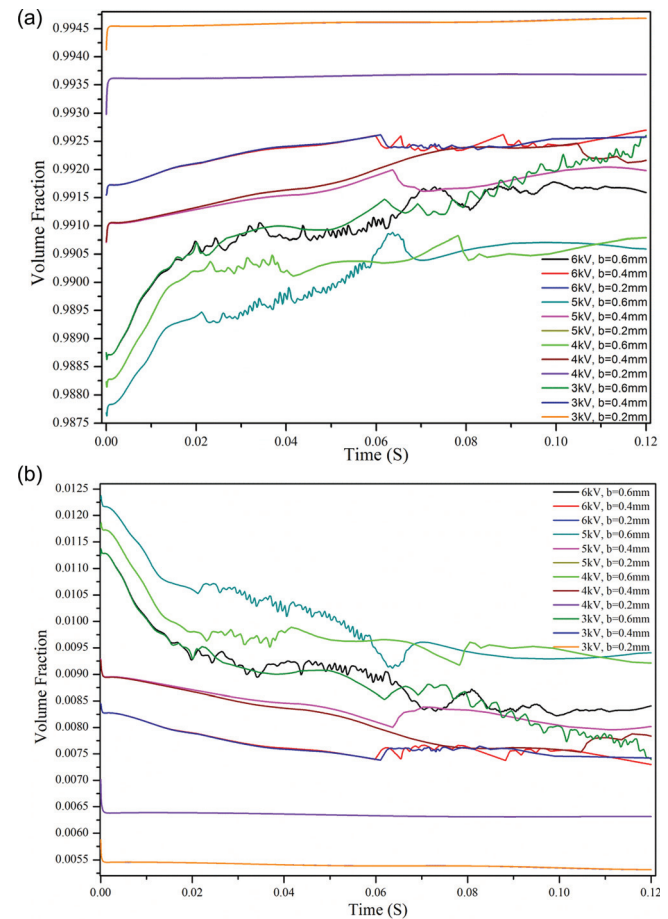


Fig. 11. (a) Variation of air volume fraction with time at different b values. (b) Variation of helium gas volume fraction with time at different b values.

the surface at different times. The results are shown in Figs. 12(a)–12(d). When a larger volume of the plasma plume was injected onto the surface, the increase in the velocity of the surface boundary would be larger. The surface velocity at the injection point was the largest when compared to other positions. The effect was well distinguishable until 4 mm away from centerline of injection.

As shown in the schematic diagram depicted in Fig. 4, the curvature of the plume surface from the tip to $50\ \mu\text{m}$ above the tip could be treated as the contact length of the gas–liquid interface. A sensitivity study was performed to examine the dependence of the velocity with which this boundary moves on the (curved) distances from the plume tip, with the b values and time as influencing parameters. The results were shown in Figs. 13(a)–13(d). Larger b values such as

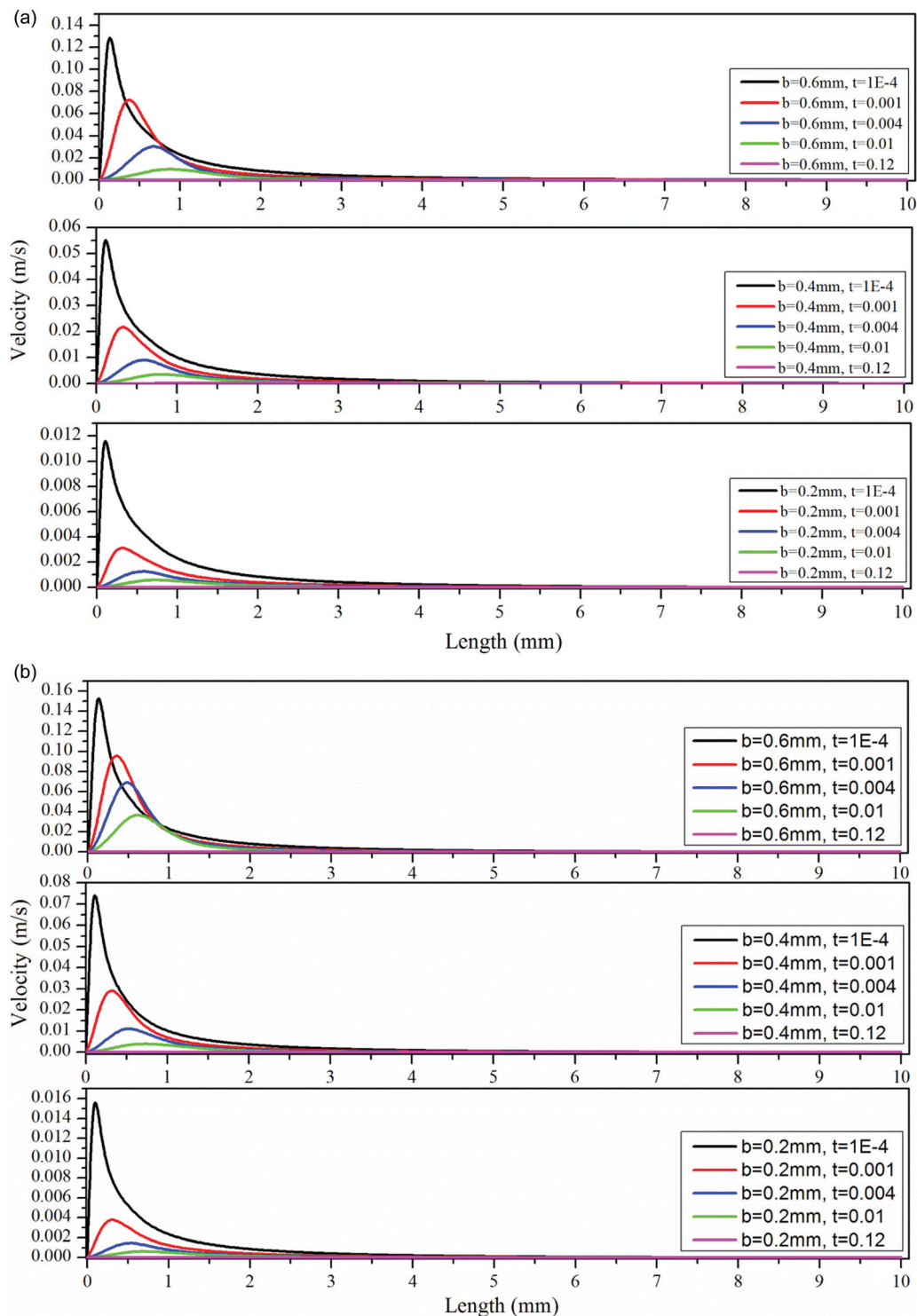


FIG. 12. Medium interface velocity change vs interface length at different times and plume volume at (a) 6 kV, (b) 5 kV, (c) 4 kV, and (d) 3 kV.

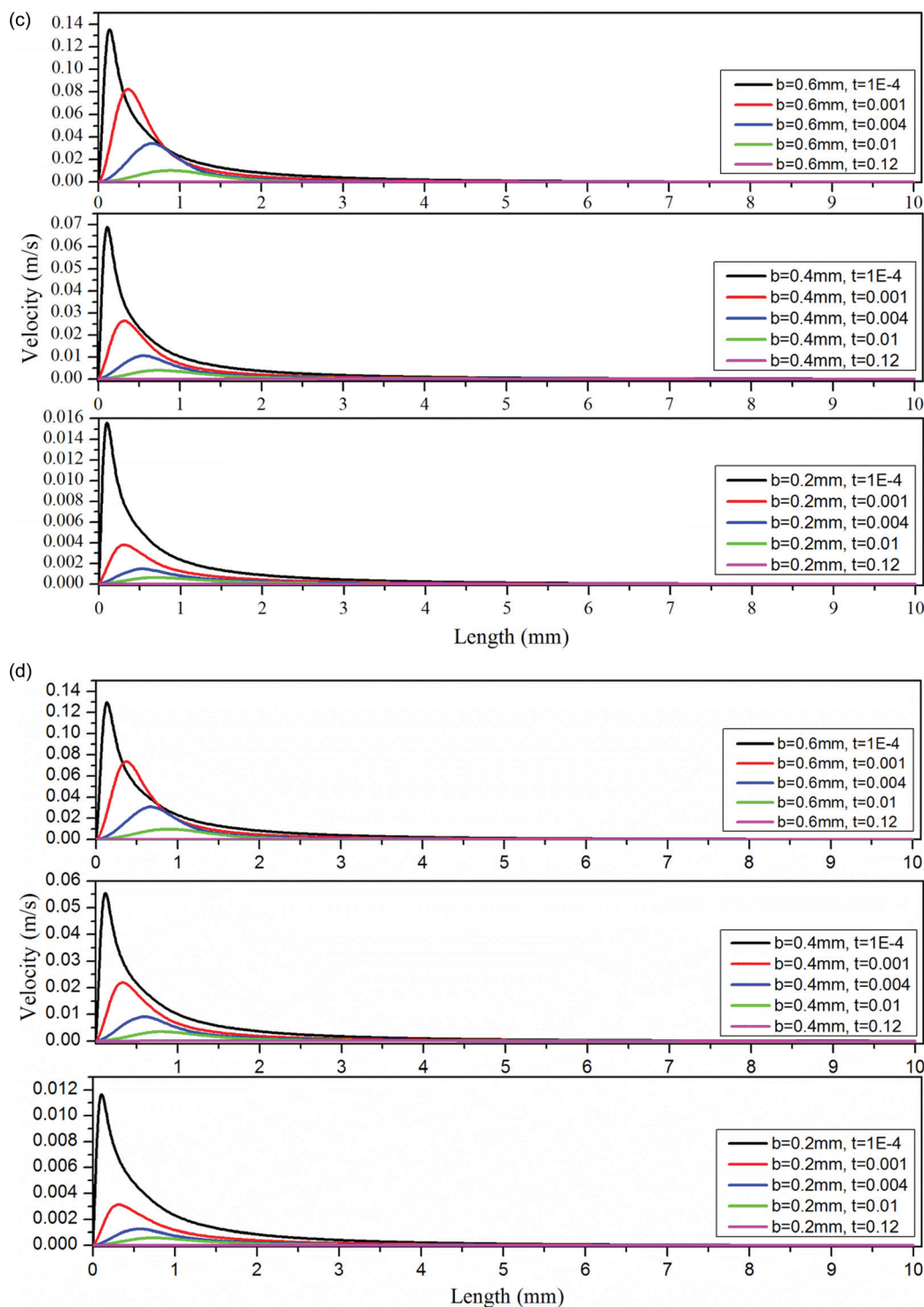


FIG. 12. (Continued).

0.6 mm corresponded to longer curvature length so the velocities at different curved distances from the tip would be higher. However, the velocity was significantly reduced when the plume impacted onto the medium surface. For smaller b values such as 0.2 mm, the initial velocities of the curved boundary were not as high as those for larger b values, so the reduction loss in the velocities upon impact onto the medium surface would not be substantial.

IV. CONTOUR PLOTS AND GRAPHICAL REPRESENTATIONS

In order to facilitate easier visualization of the systems, snapshots for the distributions of volume fraction of carrier gas, velocity, and temperature in grid 1 were shown in Figs. 14, 15, and 16, respectively, which were computed for the operating voltage of 5 kV leading to a plasma plume temperature of 30 °C and a b value of 0.6 mm.

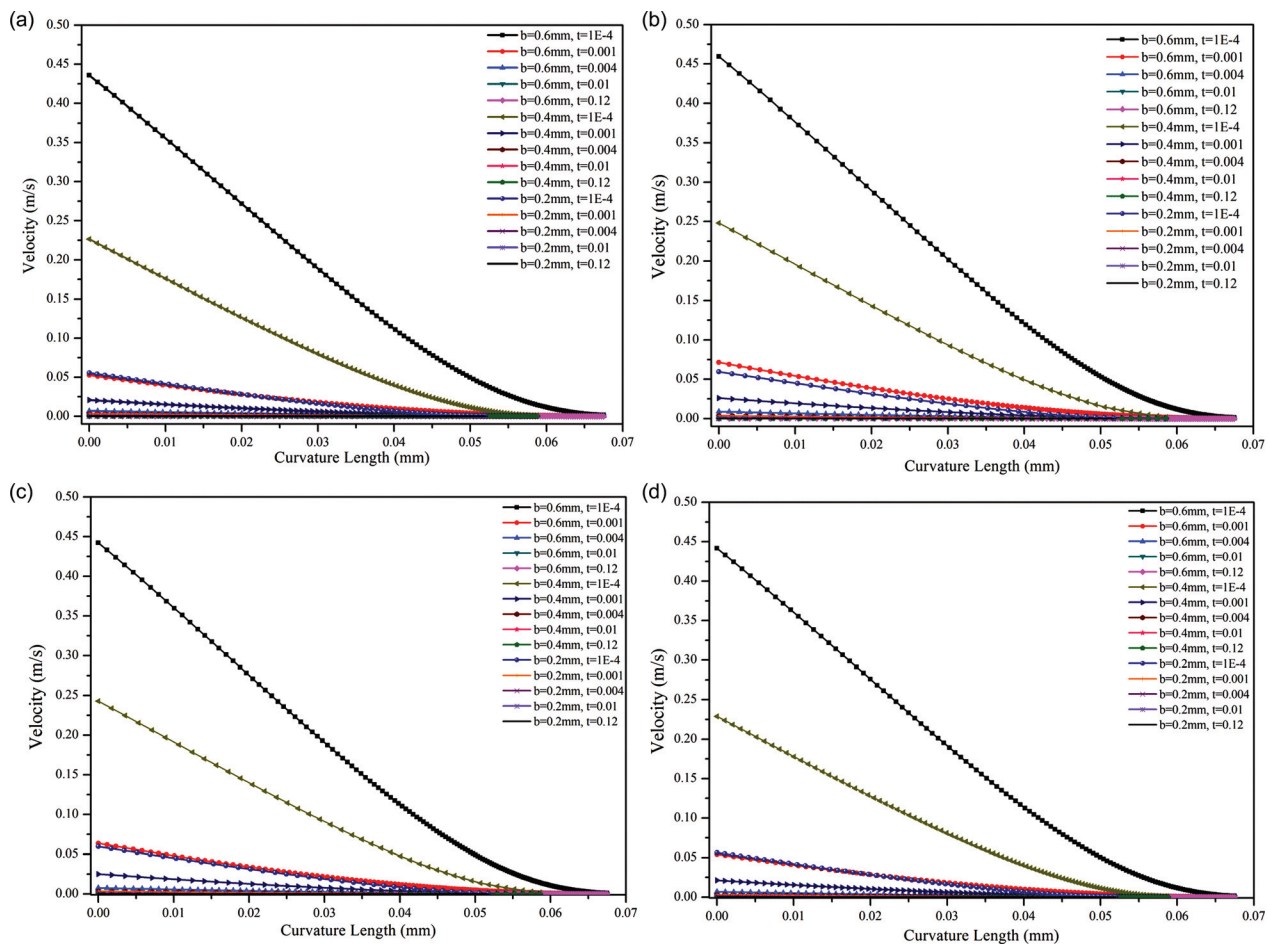


FIG. 13. Plasma plume tip velocity vs curved distance from plume tip at (a) 6 kV, (b) 5 kV, (c) 4 kV, and (d) 3 kV.

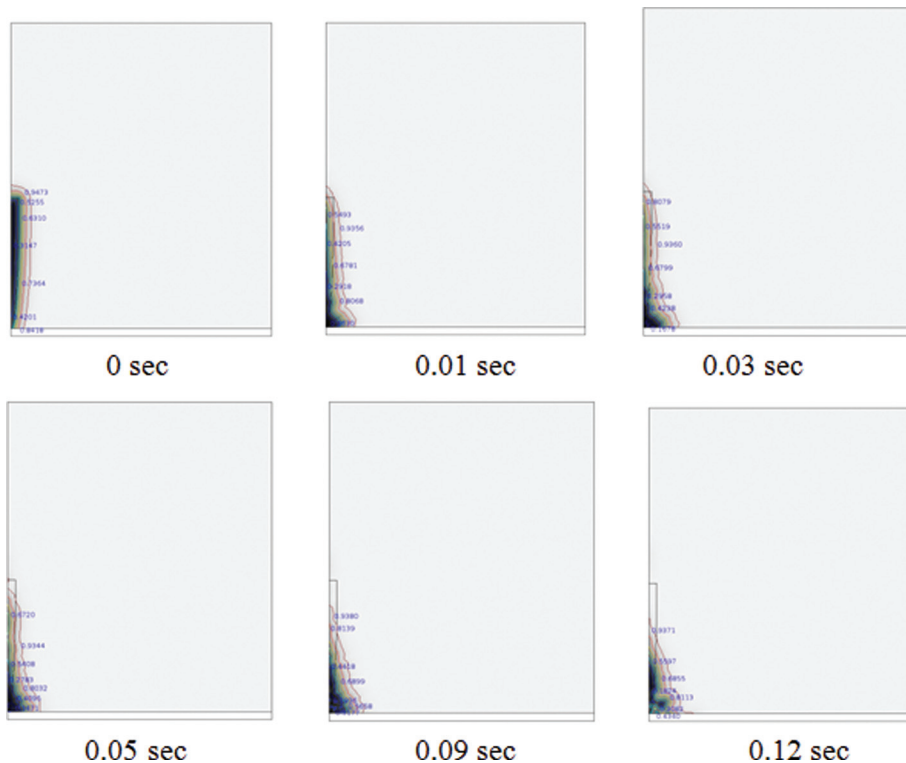


FIG. 14. Distribution of volume fraction of carrier gas in grid 1.

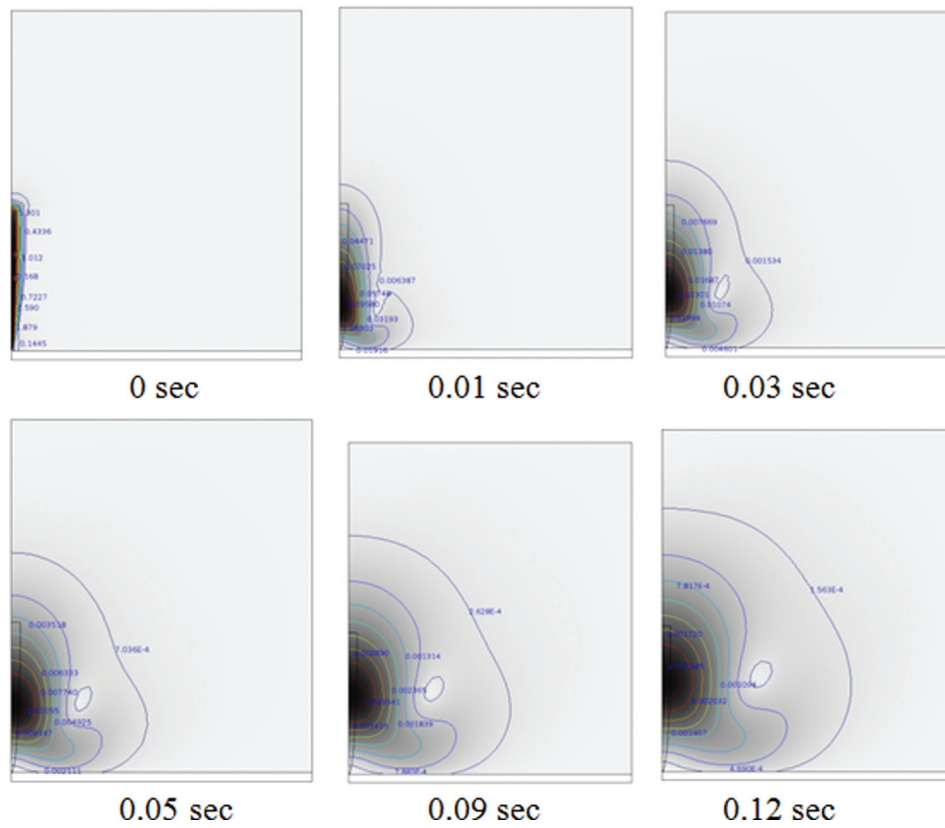


FIG. 15. Velocity distribution in grid 1.

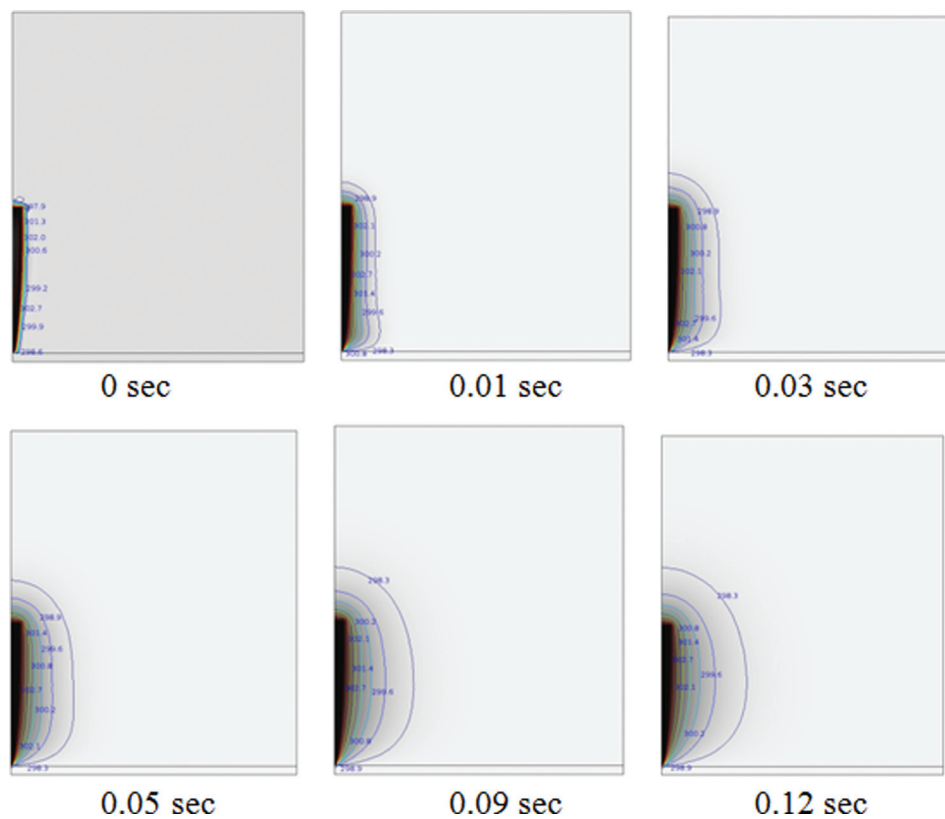


FIG. 16. Temperature distribution in grid 1.

V. SUMMARY AND CONCLUSIONS

In cold plasmas, the fraction of neutrals is much larger than that of charged species so the carrier gas could be considered the main component. For many successful biological applications of cold plasmas, the carrier gas should provide a pathway to transport the charged species to a separate medium. As such, it would be essential to have a complete thermofluid analysis of the carrier gas when it interacts with different types of fluids.

Our analysis showed the changes in the volume fraction of the plasma carrier gas as the latter interacted with air and the medium. In addition, the temperature of the concerned media was carefully monitored with very high sensitivities. The current models would be very useful for future design of plasma medicine devices and procedures involving cold plasmas.

ACKNOWLEDGMENT

The work described in this paper was supported by the University Grants Committee's Teaching Development Grant.

¹G. Fridman, G. Friedman, A. Gutsol, A. B. Shekhter, V. N. Vasilets, and A. Fridman, *Plasma Processes Polym.* **5**, 503 (2008).

²G. Y. Park, S. J. Park, M. Y. Choi, I. G. Koo, J. H. Byun, J. W. Hong, J. Y. Sim, G. J. Collins, and J. K. Lee, *Plasma Sources Sci. Technol.* **21**, 043001 (2012).

³M. Laroussi, *IEEE Trans. Plasma Sci.* **43**, 703 (2015).

⁴D. Graves, S. Hamaguchi, and D. O'Connell, *Biointerphases* **10**, 029301 (2015).

⁵E. Stoffels, I. Kieft, and R. Sladek, *J. Phys. D: Appl. Phys.* **36**, 2908 (2003).

⁶E. Stoffels, A. J. M. Roks, and L. E. Deelman, *Plasma Processes Polym.* **5**, 599 (2008).

⁷I. Kieft, J. Broers, V. Caubet Hilloutou, D. Slaaf, F. Ramaekers, and E. Stoffels, *Bioelectromagnetics* **25**, 362 (2004).

⁸G. Fridman, A. Shereshevsky, M. M. Jost, A. D. Brooks, A. Fridman, A. Gutsol, V. Vasilets, and G. Friedman, *Plasma Chem. Plasma Process.* **27**, 163 (2007).

⁹W. Kim, K. C. Woo, G. C. Kim, and K. T. Kim, *J. Phys. D: Appl. Phys.* **44**, 013001 (2011).

¹⁰P. Babington, K. Rajjoub, J. Canady, A. Siu, M. Keidar, and J. H. Sherman, *Biointerphases* **10**, 029403 (2015).

¹¹J. Hou, J. Ma, K. N. Yu, W. Li, C. Cheng, L. Bao, and W. Han, *BMC Genomics* **16**, 435 (2015).

¹²M. Laroussi, S. Mohades, and Nazir Barekzi, *Biointerphases* **10**, 029401 (2015).

¹³A. Schütze, J. Y. Jeong, S. E. Babayan, J. Park, G. S. Selwyn, and R. F. Hicks, *IEEE Trans. Plasma Sci.* **26**, 1685 (1998).

¹⁴R. Tiede, J. Hirschberg, G. Daeschlein, T. V. Woedtke, W. Vioel, and S. Emmert, *Contrib. Plasma Phys.* **54**, 118 (2014).

¹⁵M. Schröder, A. Ochoa, and C. Breitkopf, *Biointerphases* **10**, 029508 (2015).

¹⁶M. Akhlaghi, H. Rajayi, A. Shahriar Mashayekh, M. Khani, Z. Mohammad Hassan, and B. Shokri, *Biointerphases* **10**, 029510 (2015).